Article

Not peer-reviewed version

Physics-Based Hazard Assessment Of Anthropogenic Seismicity

Reza Rahemi *

Posted Date: 12 May 2025

doi: 10.20944/preprints202504.2596.v3

Keywords: Bayesian; Geophysical Data Analysis; Seismicity; Data Assimilation; Anthropogenic Seismicity; Complex Systems

Article

Physics-Based Hazard Assessment of Anthropogenic Seismicity

Reza Rahemi

Scripps Institution Of Oceanography, La Jolla, CA, 92037, United States

Abstract: Since the year 2001 and after decades of steady Magnitude ≥ 3 earthquake rate in the United States, the number of annual earthquakes have been increasing exponentially from a steady 20 events per year in that year to up to 188 events per year in 2011. This is suspected to be human-induced. Modern tools of physics such as statistical mechanics and complexity can shed light on processes which trigger seismicity, anthropogenic and otherwise. In this study, after introducing the methods of analysis, I have particularly examined anthropogenic processes such as wastewater and CO_2 injections which can trigger seismicity. Furthermore, statistical Modeling of fluid injection/extraction has been made possible using Bayesian inference. The San Andreas Fault (SAF) and the lake-fillings nearby (Salton Sea) is also chosen as a complex system of interest. Short-term forecasting of anthropogenic seismic events may be effective in mitigation strategies near fault zones.

Keywords: bayesian; geophysical data analysis; seismicity; data assimilation; anthropogenic seismicity; complex systems

---

1. Introduction

Anthropogenic activities induce seismicity and this adds to the complexities Geophysicists face when they try to understand the exact physical processes that cause earthquakes. In the case of seismicity caused by carbon capture and storage, such quakes can threaten the integrity of the seals and undermine the whole CCS operations, which by themselves are costly operations. Deformation of Earth's crusts which translate into earthquakes involve many-body problems and hence the emergence of a complex system. As an alternative approach to earthquake mechanics, Turcotte and Malamud have proposed that the tools of complexity rooted in statistical physics are capable of describing faults as a self-organizing complex system [1]. The San Andreas Fault is an example of such complex system in seismology, extending about 750 miles across central California (Figure 2.) Radiocarbon dating methods performed on this fault reveal the history of at least 10 episodes of large earthquakes on average every 132 years, ranging from the year 671 to January 9 1857 (with an estimated magnitude of 8.25) [2]. The PDF for these events as well as empirical and CDF fits are plotted and shown in Figure 1.

The absence of large earthquake episodes since, is explained using the theory that the fault-zone material do not heal after each de-formation and they lack strength needed to cause more destructive movements [3].

Tectonic faults behavior analysis is the central problem to geophysics and seismology [4–6] and therefore probabilistic hazard assessments require data assimilation and careful geophysical data analysis, which extend beyond the tools of complexity alone. Modern computational approaches to address fault analysis, such as Monte Carlo Markov Chain and Bayesian Inference are also rooted in statistical physics. In this study, these tools will be used to analyze fault behaviors in the presence of external factors such as hydrologic loads and anthropogenic activities (ranging from wastewater disposal to CO_2 induced seismicity, which are known to trigger earthquakes [7], in an attempt to guide better policy recommendations.

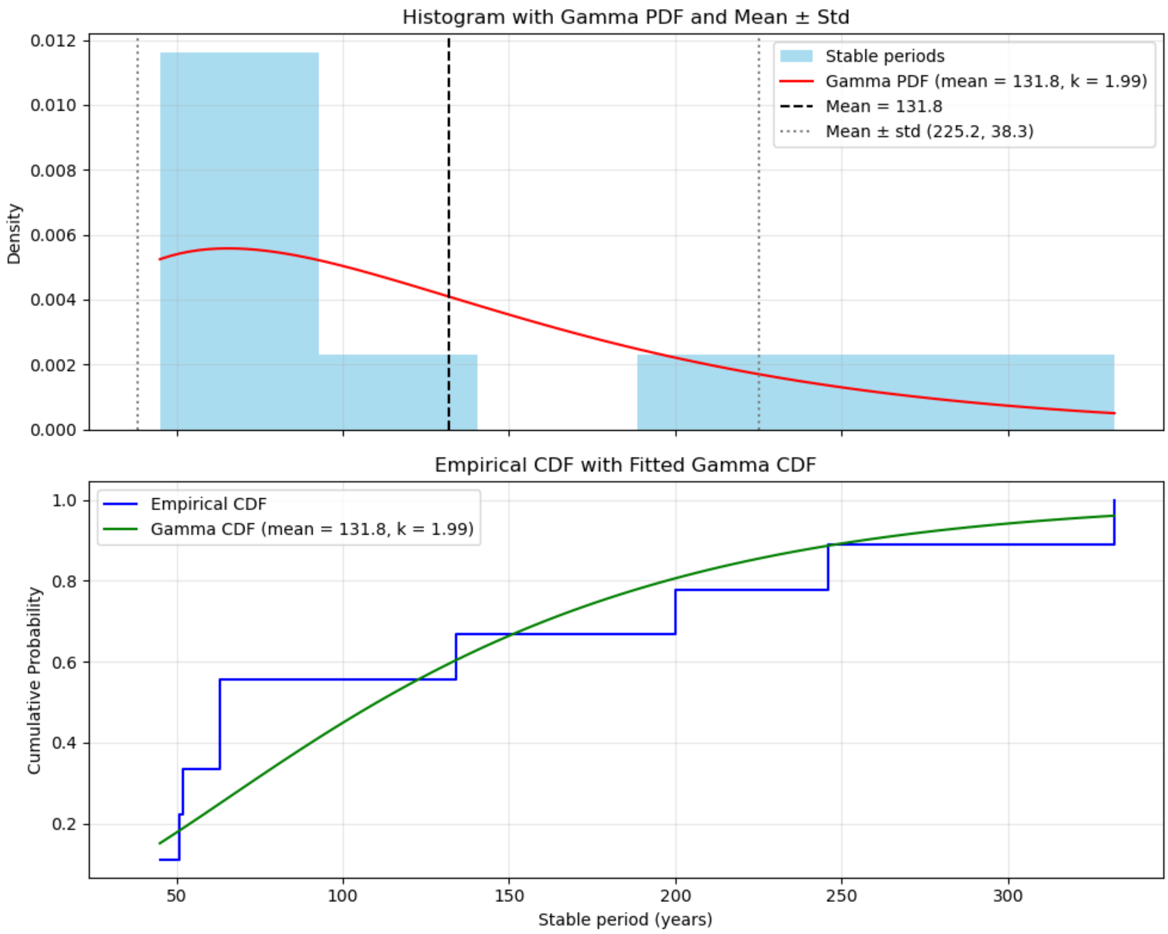

Figure 1. PDF (Probability Density Function) and CDF (Cumulative Density Function) for large earthquake events associated with the San Andreas Fault, using the raw datasets are available from Ref. [2]. The reduction in probability is explained using the theory that the fault-zone material do not heal after each de-formation and they lack strength needed to cause more destructive movements [3].

1.1. The Carbonate-Silicate Cycle

1.1.1. Earth

Walker et. al. in 1981 argued that the atmospheric CO_2 level on earth is controlled by the carbonate–silicate geochemical cycle [8] over geological timescales (Gyr). Silicate weathering also impacts the Earth's climate and carbon cycle [9], which is a key process for removing anthropogenic fossil fuel emissions over the next 10-100 Kyr in the absence of any human interventions [10–13].

1.1.2. Mars

On Mars, however, these cycles are not as well understood, given fewer experimental verifications which would require space missions for the purpose of Mars explorations (in the footsteps of NASA's Mariner 9 and Viking Missions). Nevertheless, the carbonate-silicate cycle (by a (H_2, CO_2) greenhouse gas is proposed to be the primary mechanism of Mars warming, with each cycle lasting up to 10 Myr, followed by extended periods of glaciation [14].

2. Fault Analysis: The San Andreas Fault

Markov chain Monte Carlo (MCMC) has been widely used in Earth and Environmental sciences [15–18] and even in Cosmology and Materials Science [19–21]. Liu et. al. [22] have also shown that Bayesian inference can be used in inverse modeling of contaminants and air quality modeling as well as source retrieval. To illustrate, take for instance the case of Soviet Union's Cosmos-954. A nuclear powered Satellite which crashed and fell over Canada in January 24, 1978, causing enriched uranium in several rain samples collected in Fayetteville, Arkansas to rise significantly [23]. This author will use Bayesian Inference and MCMC to determine fault parameters from geophysical data, given a geophysical model, improving our understanding of fault mechanisms which lead to seismicity (for instance to study the relative motion of the American and Pacific plates across the San Andreas fault system, as shown in Figure 2). Next, the model will be validated against the collected data and the corresponding RMSEs for each model will be calculated.

Figure 2. An aerial view of a segment of the San Andreas Fault System in Central California. It extends roughly 750 miles between (33°N, 115.5°W) and (39°N, 124.5°W). Photo: [24].

2.1. The Inverse Problem: Why MCMC?

An inverse problem in science is the process (or processes) of calculating from a set of observations the causal factor(s) that produce(s) those observations [25].

$$d = [d_1, d_2, d_3, ..., d_N]^T \tag{1}$$

$$M = [M_1, M_2, M_3, ..., M_N]^T \tag{2}$$

That is to arrive at model parameters (The M Matrix), given data (The d Matrix). The complexity of this task increases with the model complexity and uncertainty. Meaning regular fitting methods would fail to produce satisfactory model parameters. Also, simple fittings do not use **prior knowledge** [1] whereas MCMC as a tool in Bayesian Inference updates beliefs about model parameters based on data [25,26].

It is noteworthy that unlike the frequentist approaches that take errors as a flaw in measurements, the Bayesian approach sees error as a feature and not a flaw. This touches on the fundamental philosophy behind using such approaches in applications such as data assimilation.

2.2. Single Fault Model

The velocity function describing fault slip is given by [27]:

$$v(x) = \frac{v_0}{\pi} \tan^{-1}\left(\frac{x - x_0}{D}\right), \tag{3}$$

Where v_0 is the fault slip rate, D is the locking depth,x_0 is the fault location, and x is the spatial coordinate.

[1] Prior Knowledge, or simply the prior: Initial probability distribution assigned to a parameter or hypothesis before observing new data

The validity of this model when applied to the San Andreas fualt, will be examined using Bayesian Inference and will be compared to the values reported in the literature. However, it is noteworthy that to date, there are several theories about whether this fault might pose risks of larger earthquakes to the surrounding areas. Smaller earthquakes experienced are explained using the theory that the fault-zone material do not heal after each deformation and they lack strength needed to cause more destructive movements [3].

2.3. Data

The creep rate GPS and InSAR data [28] is plotted and shown in Figure 3. It is noteworthy that the creep rate peaks between 35°N to 37°N, and a maximum of 31 ± 3.5 (mm/year) appears at $(36.01°\text{N}, 120.57°\text{W})$. For a better visualization of the creep rate, it is plotted against latitude and is shown in Figure 4.

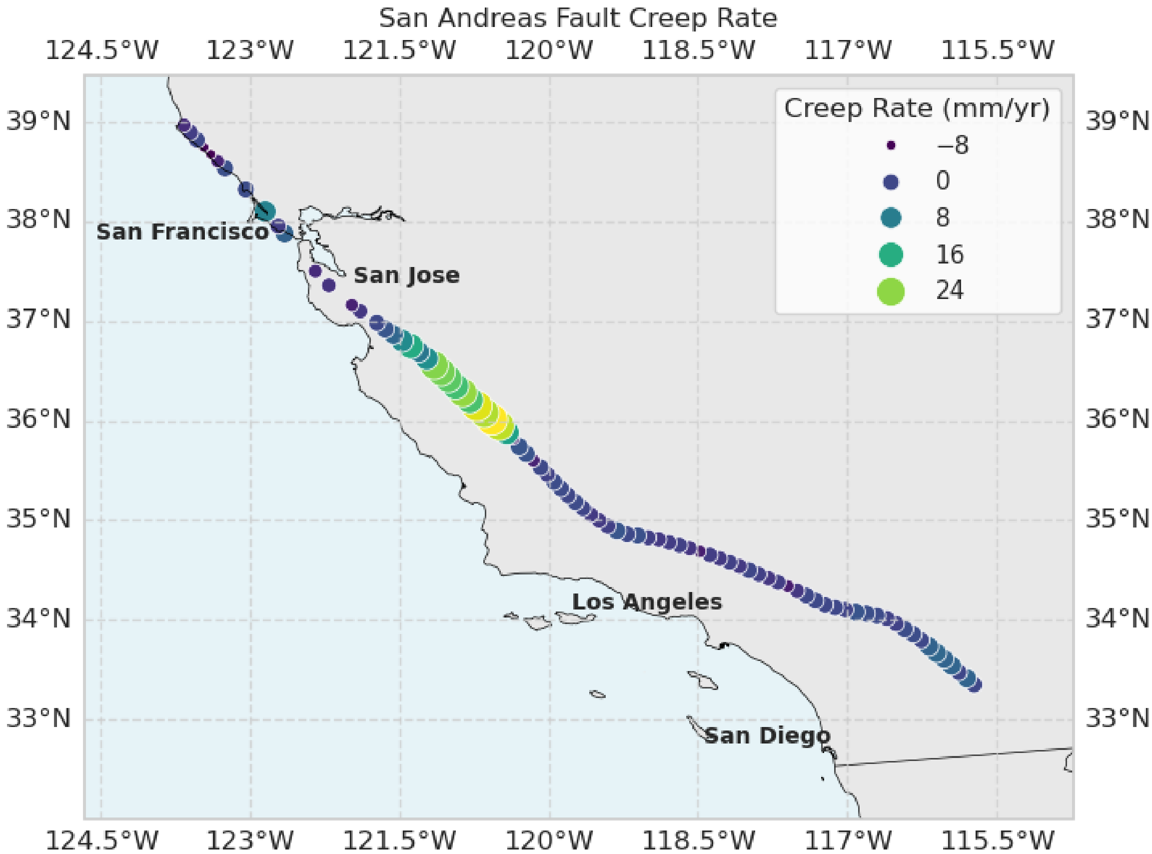

Figure 3. Location vs Creep rate data is visualized in Cartopy projection using Python. Raw datasets can be found in ref. [28]. The creep rate peaks between 35°N to 37°N, with a maximum of 31 ± 3.5 (mm/year) appearing at $(36.01°\text{N}, 120.57°\text{W})$.

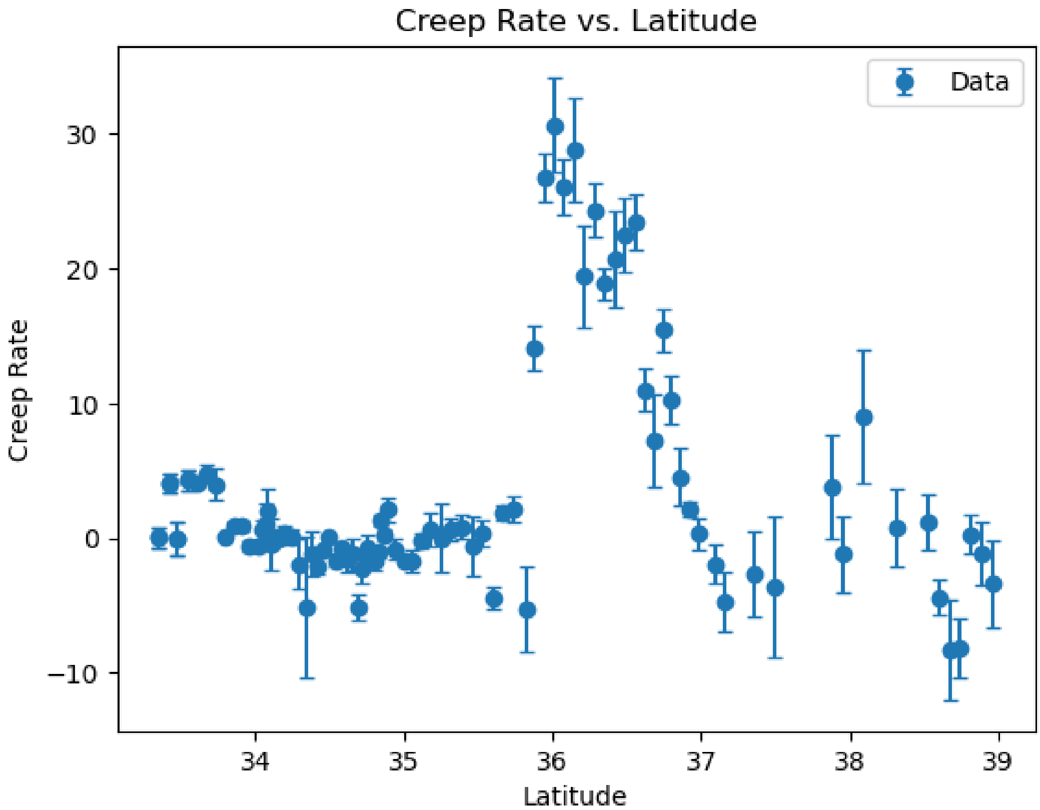

Figure 4. Creep rate vs Latitude and the corresponding uncertainties. Distributions of the uncertainties are plotted and shown in figure 6.

2.4. Gaussian Processes: GPs

A Gaussian Processes based model was fit to the creep rate data (Figure 5).

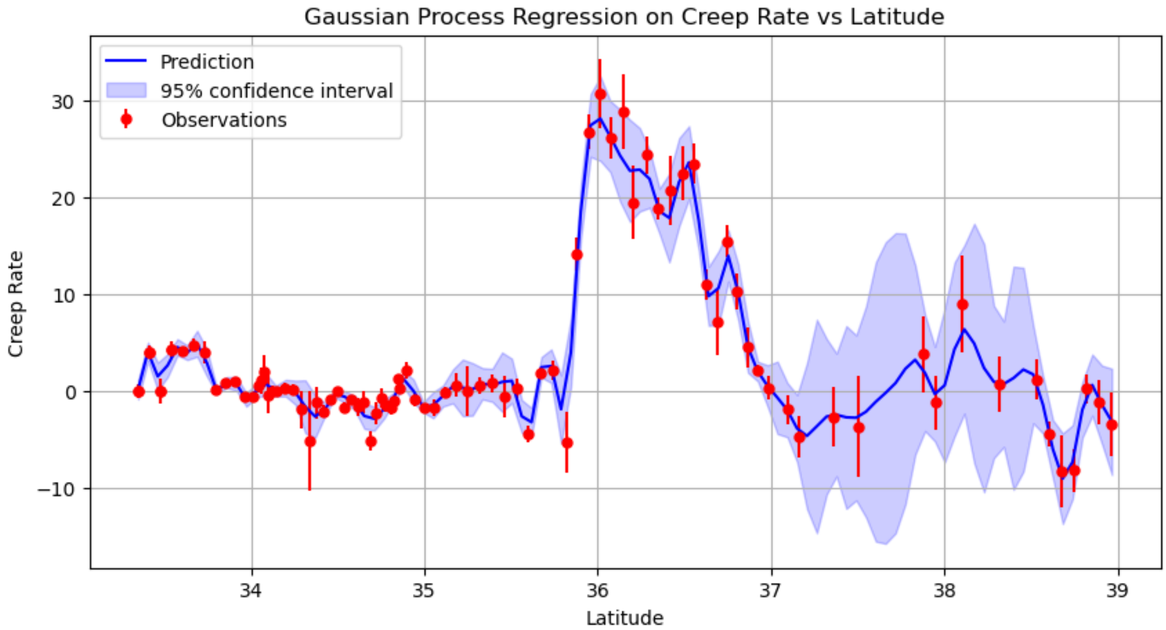

Figure 5. Creep rate model with Gaussian process regression targeting creep rate and its uncertainties. Higher creep rate uncertainties result in higher model uncertainty as well. Measurement improvements can improve the predictive model.

 doi:10.20944/preprints202504.2596.v3

2.5. *Line of Sight Velocities (LOS)*

The Line Of Sight (LOS) velocity data [29] is assumed to have a variance of 1.

Creep rate uncertainty as suggested in [28] is 1.2 ± 1 (mm/year). The distribution of this uncertainty in measurement of the creep rate is shown in Figure 6. The data is loaded from a file (available in the GitHub repository for this project), assuming a two column structure separated by commas. First column is assumed to be the x(positions) and the second is the velocities $v(x)$. We also assume the the observational errors follow a Normal distribution, $y_j = v(x_j) + \epsilon_j$ Where $\epsilon_j \sim N(0, \sigma^2)$ and STD $\sigma = 1$ with respect to the model equation given in eq. 3.

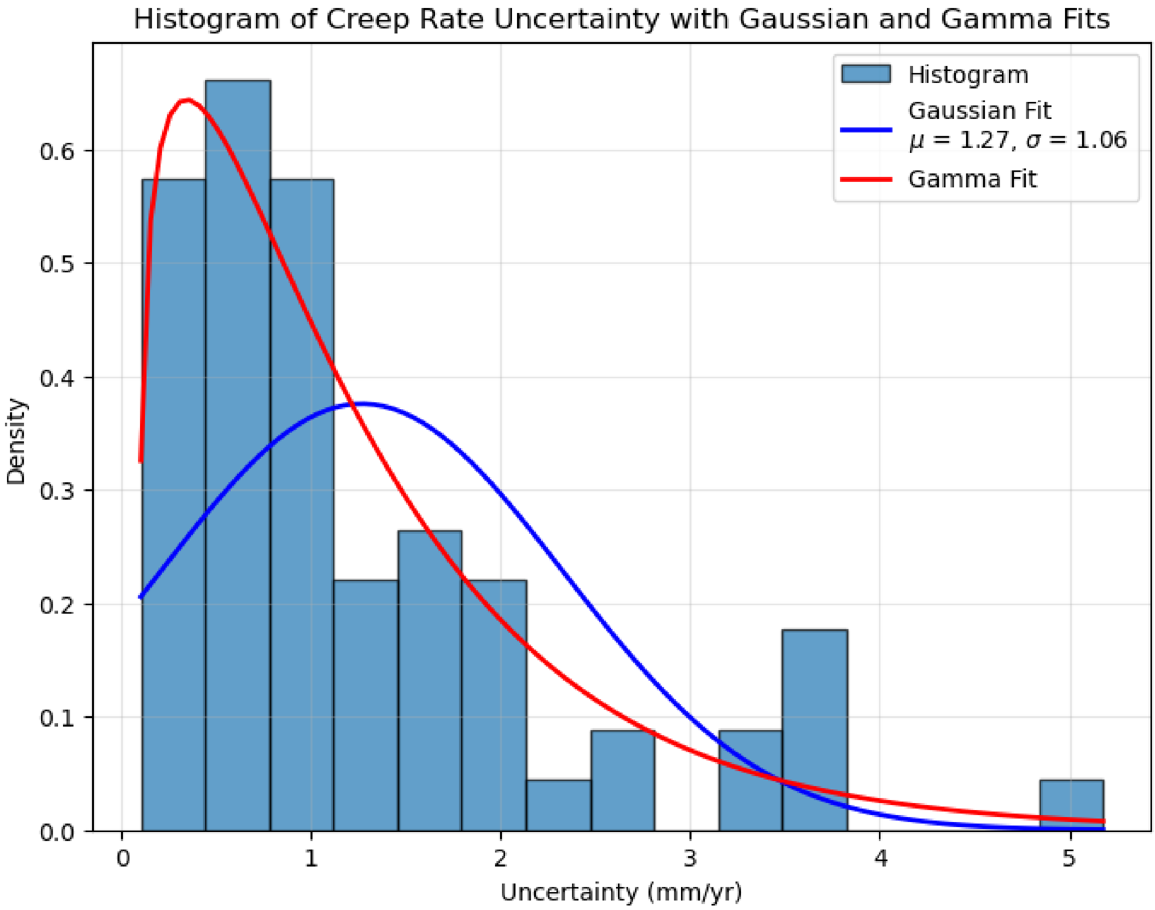

Figure 6. Creep rate uncertainty distribution plotted for San Andreas fault based on high resolution GPS and InSAR data from Ref. [28]. The Gaussian fit shows a μ of 1.27, however, given the existence of heavy tails, a Gamma fit might be a better choice to fit the uncertainty data than just using a normal distribution. Gaussian peaks around 1.27 while Gamma peaks around 0.5. In Gamma fits, the average doesn't represent the data.

2.6. *Two-Fault*

The volocities are additive (superposition of two single-faults).

2.7. *Defining Log-Likelihood and Log-Prior*

We want to know how well the model fits the data.

For Gaussian errors, the likelihood is [26,30]:

$$p(y_j|\theta) = \prod_{j=1}^{N_j} \frac{1}{\sqrt{2\pi\sigma^2}} \exp(-\frac{(y_j - v(x_j, \theta))^2}{2\sigma^2}). \tag{4}$$

When taking the Log-Likelihhood, the product becomes a sum. Given $\sigma = 1$, it simplifies to

 doi:10.20944/preprints202504.2596.v3

$$\log p(y_j|\theta) = A(-\frac{1}{2}\sum(y_j - v(x_j))^2) \tag{5}$$

Where A is a constant throughout the MCMC process.

2.8. Bayesian Context

In Bayesian Context, the Posterior distribution of the parameters given the data $p(\theta|y)$, which is our goal, is given as:

$$p(\theta|y) = \frac{p(y|\theta)p(\theta)}{p(y)} \tag{6}$$

$p(y|\theta)$ is the likelihood (How probable the observed data is under specific parameter values). $p(\theta)$ is our initial beliefs about the parameters. $p(y)$ is the Evidence, which is a normalizing constant, which can be ignored in MCMC since we are sampling ratios. So in order to find the posterior, we need to compute the likelihood, which determines how well a given set of parameters θ explains the data y.

2.9. Log-Prior, Single Fault

We have a uniform prior, where $p(\theta)$ is a constant if within bounds, and if not, zero. So log prior would be 0 if valid and $-\infty$ if not. The purpose of this is to constrain parameter ranges. For instance, v_0 and D both range between 0 and 80 while x_0 ranges from -50 to 50.

2.10. Random Walk Metropolis Sampler: Markov Chain Monte Carlo (MCMC)

$$p(\theta|y) \propto p(y|\theta)p(\theta) \tag{7}$$

This algorithm implements the Metropolis-Hastings MCMC algorithm. Starting at an initial guess, we propose a new point $\theta' = \theta + S \cdot N(0,1)$ with S being the step scale. We then compute the log-posterior by taking the log of eq. 7, we arrive at:

$$\log p(\theta|y) \propto \log p(y|\theta) + \log p(\theta) \tag{8}$$

The outputs are chain of samples, log-posterior values and acceptance rate.

2.11. Applying MCMC: Single Fault Model Analysis

The mean and STD of v_0, D, x_0 are our posterior stats. The posterior distribution and correlations are plotted in Figure 7.

The MCMC model run over 30,000 samples burn-in of 5,000, step size 1.0:

 doi:10.20944/preprints202504.2596.v3

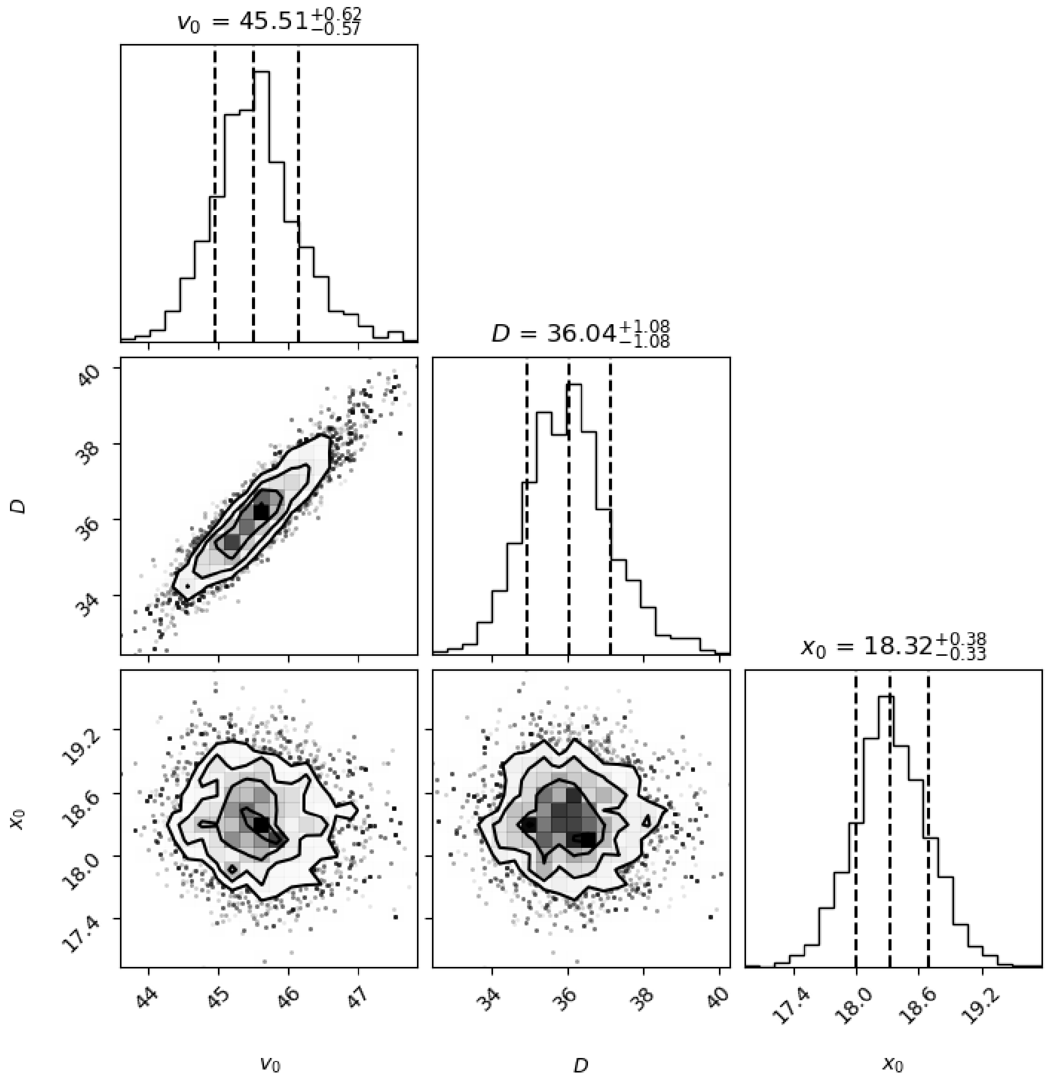

Figure 7. Posterior Plot: Visualizing the posterior distribution and correlations. Plotting data and 100 random posterior model curves. First few x values: [-97.922 41.985 95.654 -60.534 -86.19] First few v values: [-16.41 7.0886 14.671 -14.797 -16.455] Single-fault acceptance rate: 11%. Single-fault posterior means: [45.53 36.05 18.34] Single-fault posterior stds: [0.61 1.13 0.35]

2.12. Posterior Samples VS Data

Plot of the posterior samples vs Data is shown in Figure 10.

2.13. RMSE and the Two-Fault Model

The RMSE is defined as

$$\mathrm{RMSE}_i = \left(\frac{1}{N_s} \sum_{j=1}^{N_y} \left(\frac{y_j - \hat{v}(x_j, \theta_i)}{\sigma_j} \right)^2 \right)^{1/2} \tag{9}$$

where y_i are the N_y observations of the velocity, σ_j are the standard deviations of the model errors and $\hat{v}(x_j, \theta_i)$ is the velocity at location x_j, using parameters θ_i. The RMSE for single-fault model is approximately 1.4. This is not disastrous, but not ideal either. To improve this, we consider a modified version of this model, namely "Two-Fault" model and see if we can arrive at a better RMSE.

Preprints.org (www.preprints.org) | NOT PEER-REVIEWED | Posted: 12 May 2025 doi:10.20944/preprints202504.2596.v3

2.14. *The Two-Fault Model*

In this model, instead of one fault, we consider two faults. We start by two-fault velocity, generalizing equation 3. , arriving at

$$v = \frac{v_{10}}{\pi} \arctan(\frac{x - x_{01}}{D_1}) + \frac{v_{02}}{\pi} \arctan(\frac{x - x_{02}}{D_2}) \tag{10}$$

The MCMC analysis is similar to that of single-fault model. The Two Fault Model Parameters are calculated and shown in Table 1.

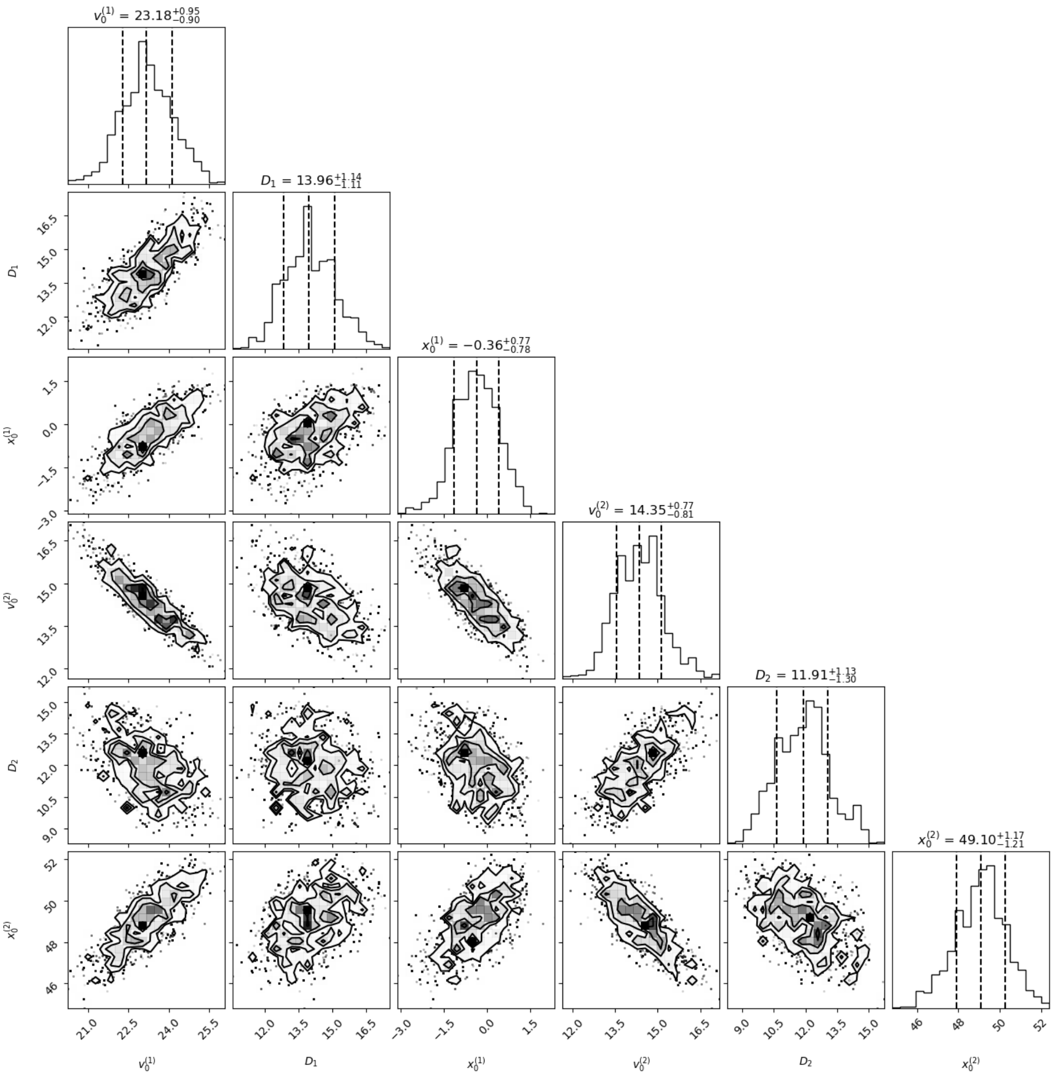

Figure 8. Triangle corner plot of two-fault model Parameters, obtained using the two-fault velocity model.

It is noteworthy that there is a negative correlation between the two velocities v_0^1 and v_0^2 and these are exclusively shown in Figure 9.

Table 1. Two Fault Model Parameters.

v_{01}	23 ± 1
v_{02}	14 ± 1
-x_{01}	0.4 ± 0.8
x_{02}	49 ± 1
D_1	14 ± 1
D_2	12 ± 1

doi:10.20944/preprints202504.2596.v3

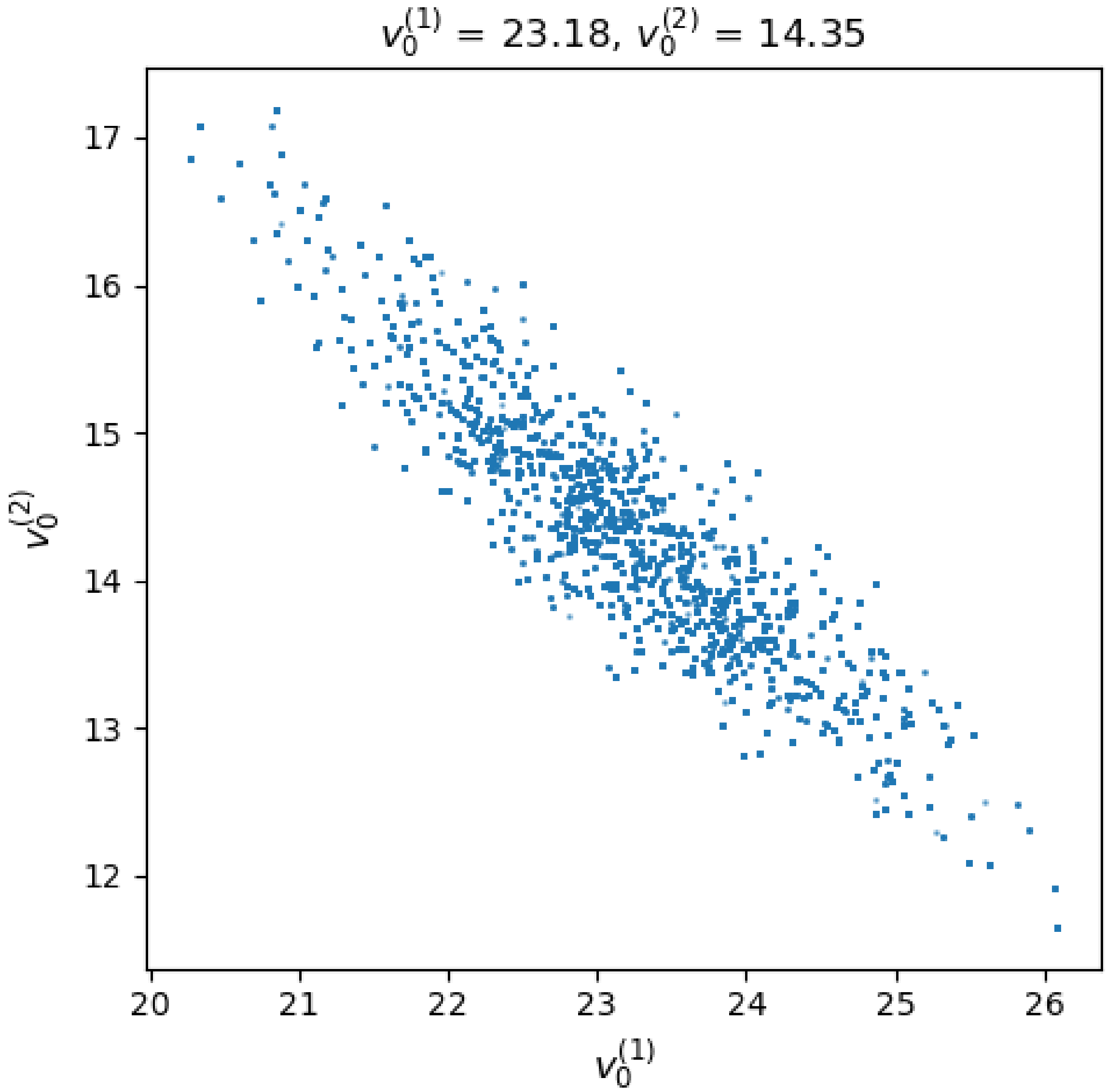

Figure 9. The negative correlation between the two velocities v_0^1 and v_0^2 are shown here.

For model validation, posterior samples are directly compared to experimental data. The error bars are not graphically displayed since they are relatively small and the points in Figure 10 overlap in representing the data and the corresponding uncertainty.

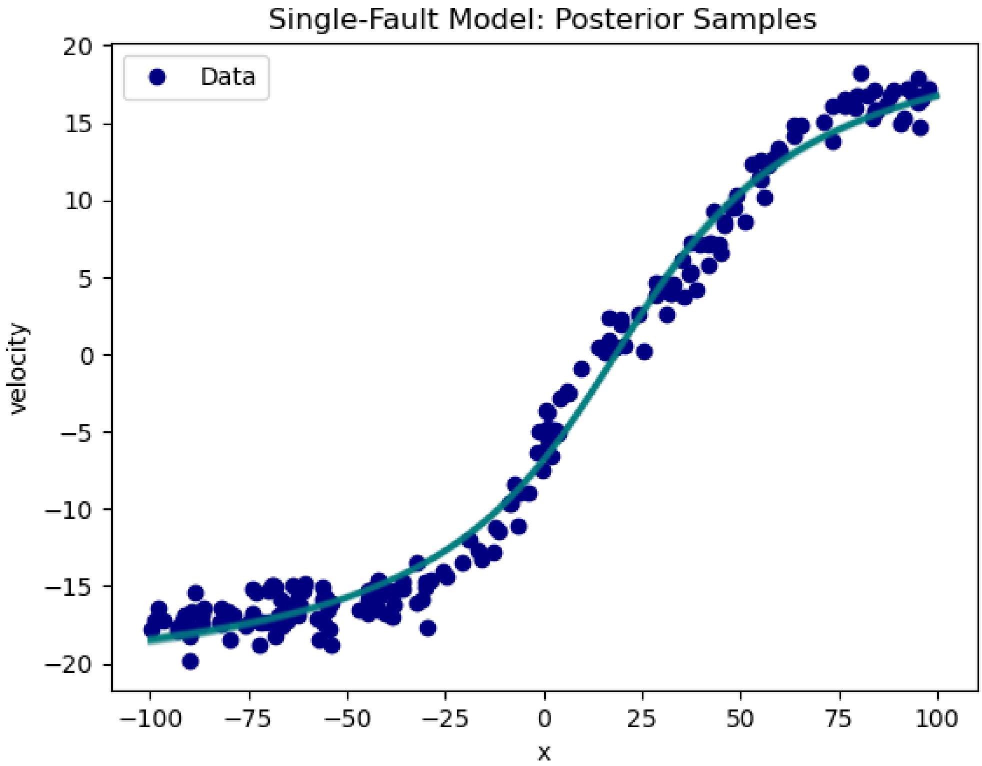

Figure 10. Posterior Samples VS Experimental Data for the geophysical single-fault model. The model fits well, but it is not ideal, given a relatively large RMSE of 1.4.

Although not very far from 1, the value of 1.4 for the RMSE is not ideal. Particularly around the origin (see fig. 10), the deviation of data from model become more obvious.

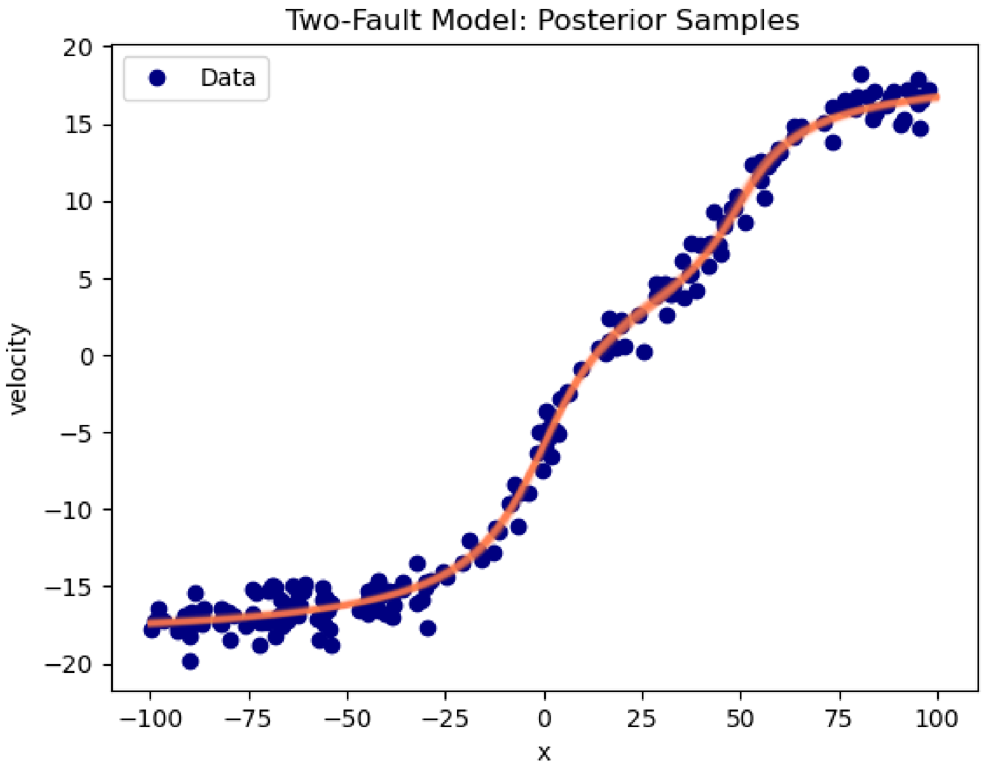

Figure 11. Two Fault Model Posterior VS Experimental Data. The RMSE is ≈ 1.

Preprints.org (www.preprints.org) | NOT PEER-REVIEWED | Posted: 12 May 2025 doi:10.20944/preprints202504.2596.v3

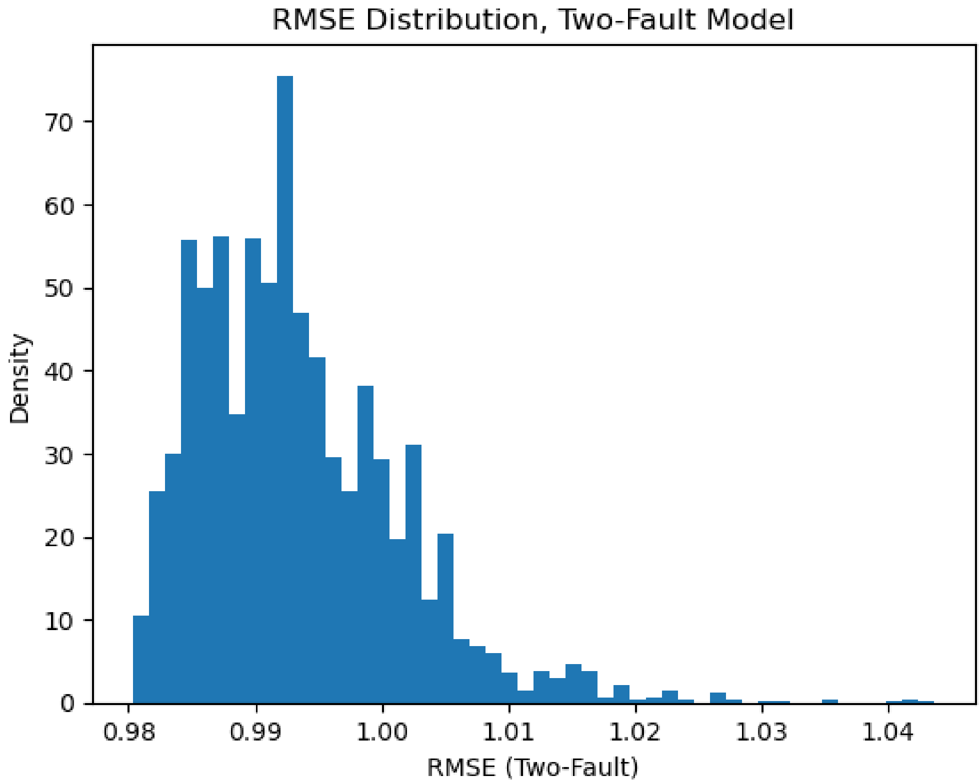

Figure 12. Two-Fault Model RMSE distribution, which is centered around value of 1.

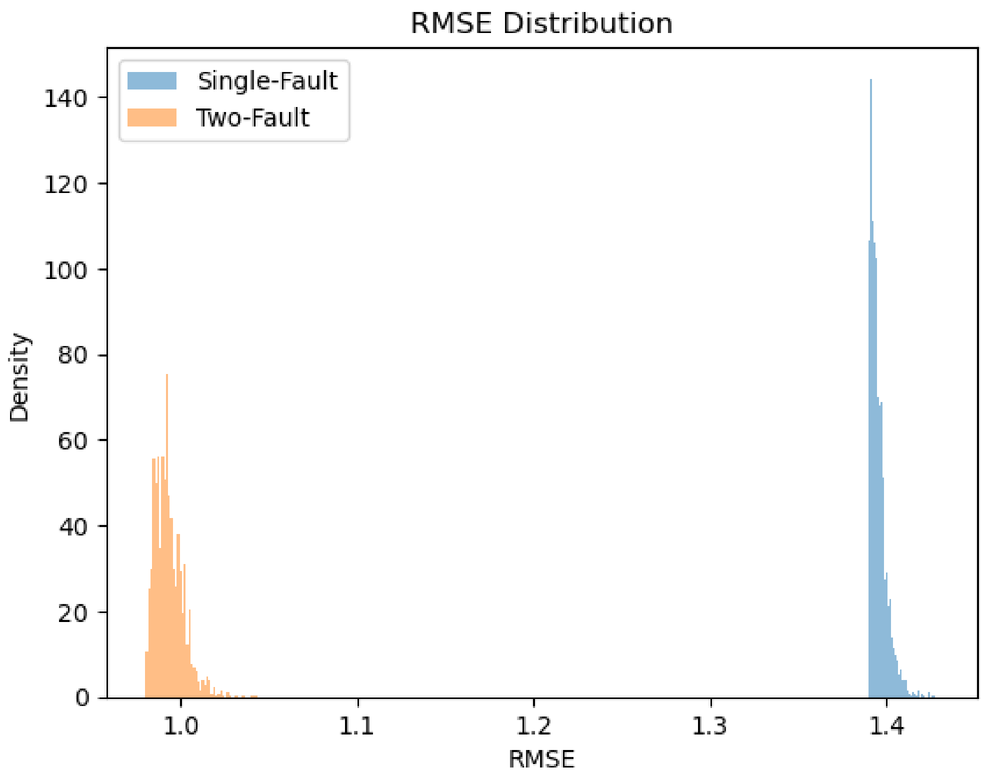

Figure 13. Two Fault Model RMSE distribution ≈ 1 (Left) VS Single Fault RMSE ≈ 1.4 (Right).

2.15. Fault Analysis: Discussion

Markov Chain Monte Carlo is a powerful method for Data Analysis. In this study, it was used as a tool in Inverse Problem, fitting model parameters to data. This geophysical model elegantly fit to

 doi:10.20944/preprints202504.2596.v3

data of 200 points. Using a single-fault model, the parameters were obtained, however with a RMSE of 1.4, which was not ideal. Therefore a Two-fault model was examined, arriving at a RMSE of 1.

Single Fault Model Parameters are displayed in Table 2.

Table 2. Single Fault Model Parameters

v_0	45.5 ± 0.6
x_0	18.3 ± 0.4
D	36 ± 1.1

Which all are within 95 % confidence intervals. These parameters and their error bars are plotted and presented in Figure 14.

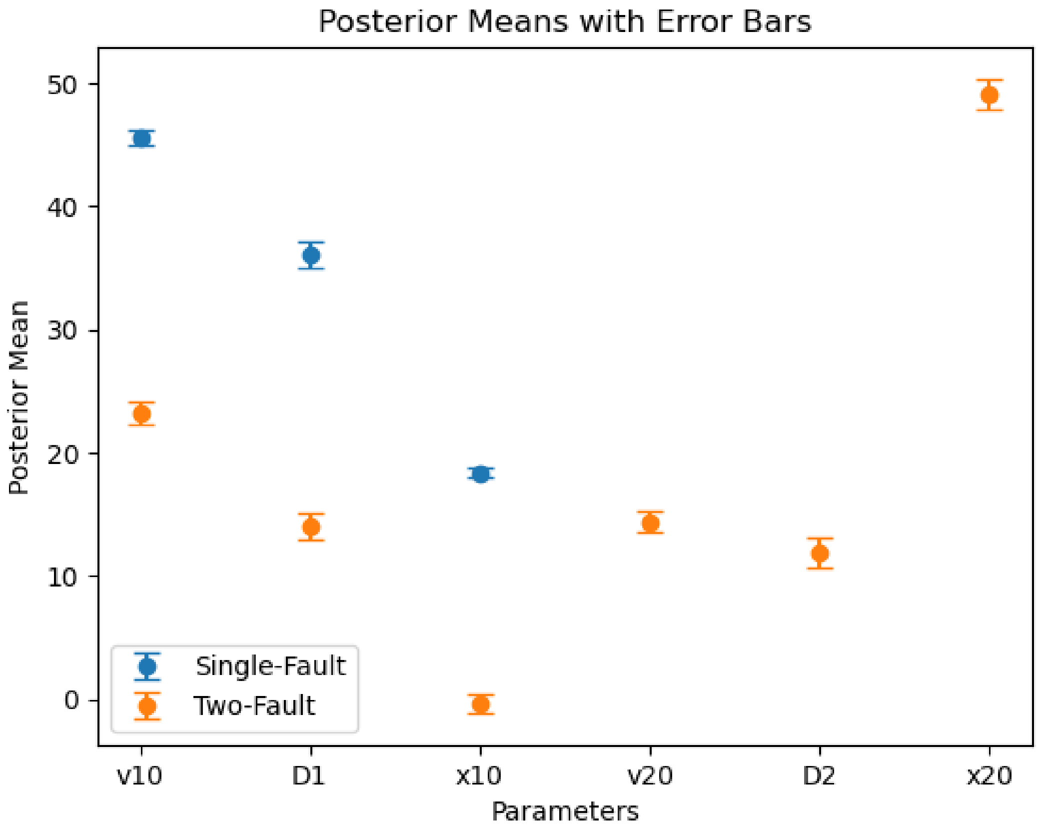

Figure 14. Model Parameter Values and their corresponding uncertainties, within 95 % Confidence Interval

The RMSE is already improved to the level of background noise and this can be easily seen comparing Figures 6 and 13. A Plot of the residuals versus the data is shown in Figure 15. A Model comparison is plotted (see Figure 15).

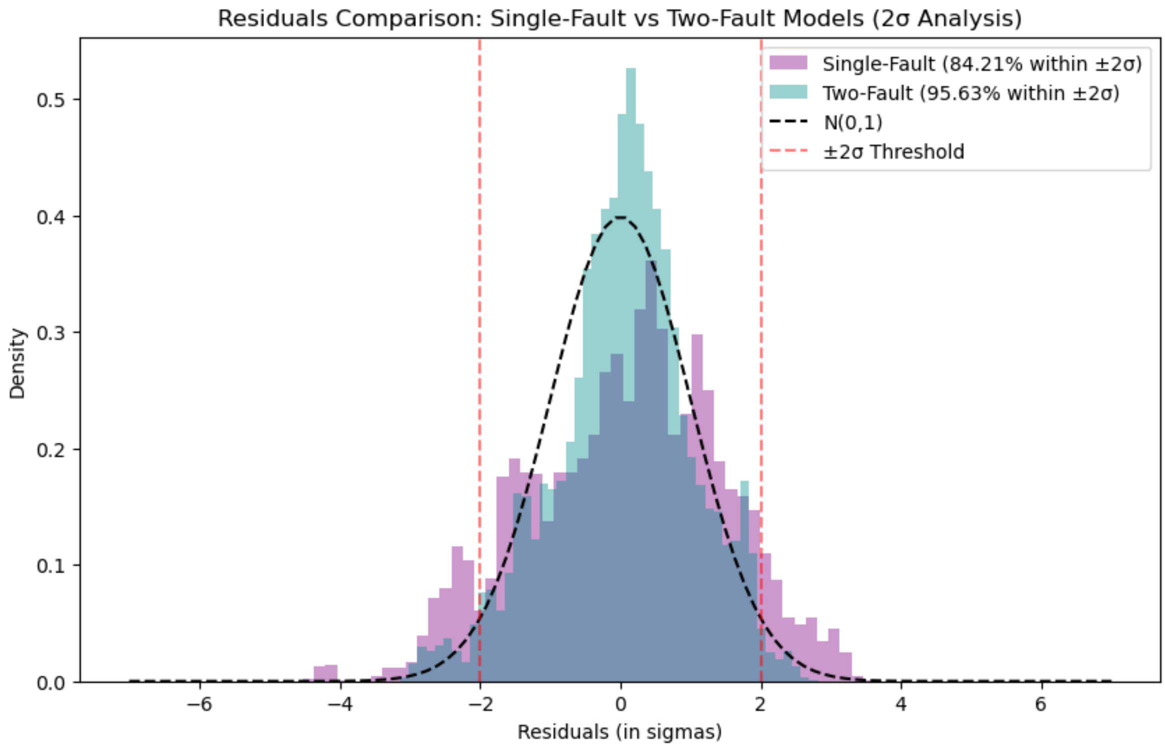

Figure 15. Comparing the residuals of the two models in terms of σs. More than 95 percent of the the two-fault model residuals are contained in a 2σ deviation interval, which is equivalent to an error of 2 mm/year with a variance of 1.

This suggests that the SAF does not act in isolation and other fault systems such as San Jacinto fault (SJF) in southern California contribute to the velocity field. The $v_0^{(2)} = (14 \pm 1)$ is consistent with the the SJF velocity rate of (11 ± 4) mm/yr reported by Rockwell et al. [31].

3. Anthropogenic Seismicity

Under load, soil does not instantaneously deflect, but changes gradually and at a variable rate. This phenomenon is called **consolidation** and is mathematically formulated by Biot in 1940 [32]. Hill et. al.[33] argue that stress perturbations in the order of **0.5 MPa** are sufficient to trigger seismicity. These perturbations are dominated by pore pressure changes. They furthermore correlated the past 6 major earthquake events on the San Andreas Fault with high-stands of the ancient Lake Cahuilla, which its remnant is known today as the Salton Sea. Using Finite Element Methods (FEM) to arrive at such correlations, their model seems to be applicable to other regions where hydrologic loading is associated with seismicity, anthropogenic or not.

The anthropogenic seismicity risk factor, which I will define as $\bar{R}$ here, (With the physical units of action per unit volume), generally follows an uncertainty relationship:

$$\Delta p \Delta t \geq \bar{R} \tag{11}$$

Where Δp represents the change in pressure and Δt is the time period, with $\bar{R}$ resembling the system's minimized action per unit volume. This is due to the fact that higher pressures of fluid injections are usually carried out over shorter periods of time and lower pressures are carried out over a larger period of time. In other words, there is a tradeoff. For instance, a larger pressure of wastewater is injected over a short period of time while a smaller pressure of CO_2 is associated with CCS operations over longer periods of time. When examined as a complex system, this resembles a path which constraints the system's evolution in which soil consolidation undergoes dissipation.

A breakdown of these operations and their corresponding share of caused anthropogenic seismicity can be found in figure 16.

 doi:10.20944/preprints202504.2596.v3

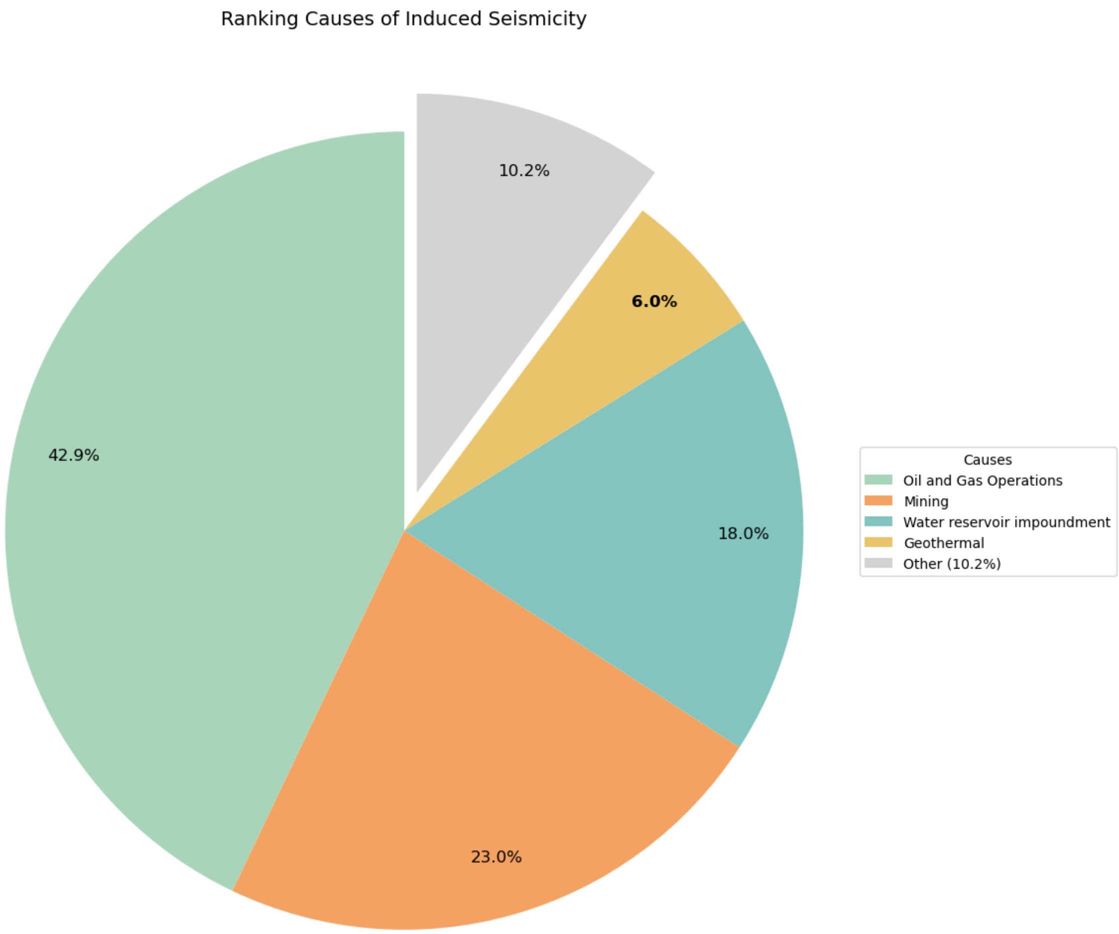

Figure 16. The share and recorded causes of anthropogenic earthquakes.Raw data can be found in Human Induced Earthquake Database (Hiquake) [34].

3.1. Oil and Gas Operations

The probability of reservoir-seismicity to be widespread and deeper for a large reservoir is higher than that of a small one [35]. Elevated seismicity in Texas attributed to oil and gas extraction and fluid injections has also been observed [36], which is thought to be caused by pore pressure changes.

It is noteworthy that the Los Angeles Oil Field produces about 3.5 barrels of oil per day and also faster than 1 $mm/year$ LOS movement on the fault [37].

3.2. CCS & Wastewater

CO_2 also stimulates plate tectonics due to mechanical pressure excreted by the injected fluids. In the past few years, as part of broader mitigation efforts, CO_2 has been injected into the earth. It is postulated that the injected CO_2 stays underground for decades. The pressure excreted by this gas can however threaten the integrity of the seals at injection sites. This requires further analysis on the operations as well as more simulations which could shed light on anthropogenic seismicity caused by geological injections. Zoback et. al. argue that in order to reduce the risk of seismicity from such operations, the Δp (pressure), as shown in my uncertainty relationship (11), should be limited. Increasing pressure can also trigger an earthquake and as a result, threaten the integrity of the CCS seals. A map of areas in the United States with active or potential CCS operations is shown in figure 17.

Preprints.org (www.preprints.org) | NOT PEER-REVIEWED | Posted: 12 May 2025 doi:10.20944/preprints202504.2596.v3

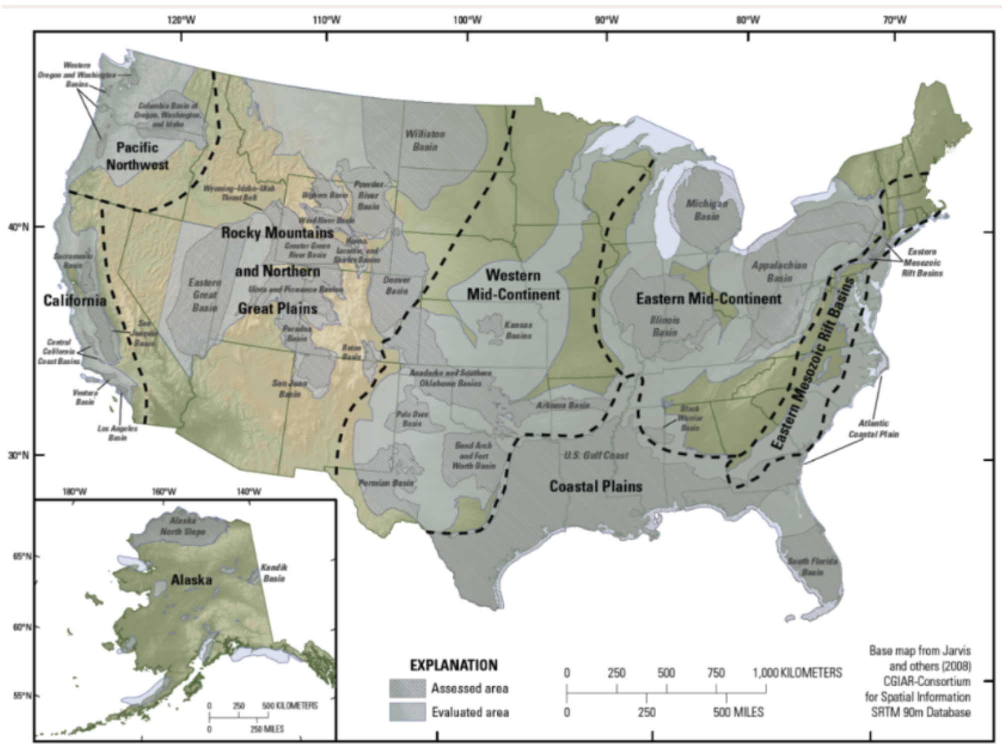

Figure 17. The map of areas in the United States with active or potential CCS operations. Oklahoma is particularly vulnerable to such operations. Carbon dioxide pipelines also pose risks to communities. Additionally, the construction and operation of such infrastructure can lead to environmental damage beyond control in absence of effective risk monitoring. This may inadvertently lead to public distrust in such operations. Induced seismicity, when uncontrolled, can also threaten the integrity of the seals and undermine the CCS operations. Involving communities might mitigage those risks. Adopted from [38].

4. Extreme Event: The 1906 San Francisco Earthquake

The Earth has been through numerous extreme events. From Geomagnetic reversals to super-volcanic eruptions. These events are rare, but have shaped Earth's history profoundly. As an example, a geomagnetic reversal timeline is plotted in figure 18.

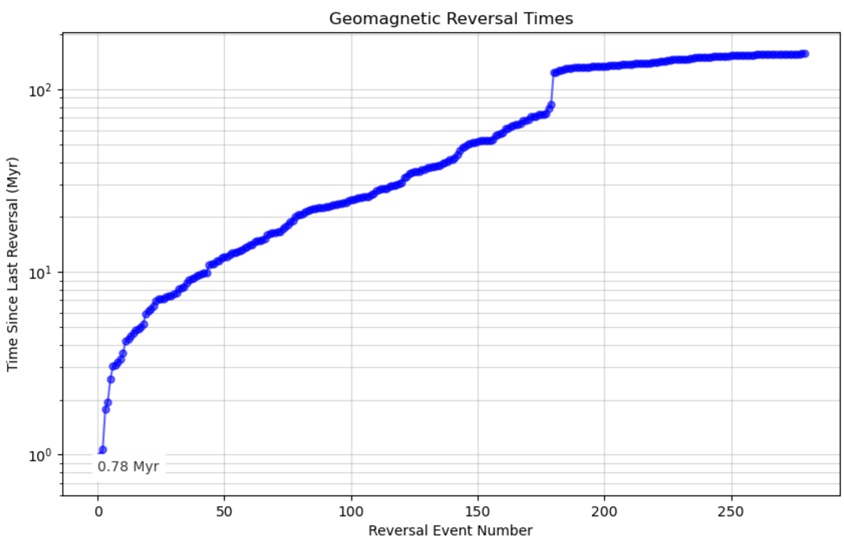

Figure 18. Geomagnetic reversal timeline. The last reversal happened around 0.78 MYrs ago, with the probability of reversals decreasing with time.

Preprints.org (www.preprints.org) | NOT PEER-REVIEWED | Posted: 12 May 2025 doi:10.20944/preprints202504.2596.v3

Following the 1905 Salton Sea filling when the Colorado river flooded into the Salton sink (southern end of the SAF) due to extreme flooding after a policy error, San Francisco experienced an earthquake of magnitude 7.9 in 1906 which left more than 3000 casualties. Supported by paleo-seismic data, major SAF earthquakes are shown to be modulated by ancient lake-fillings [33].

5. Sea Level Rise

Global increase in seismic activity is thought to be related to sea level rise. In fact Tectonophysics studies have shown that seismicity can contribute to the relative sea level change, which currently has the velocity of about (1.75 ± 0.55) mm/year [39]. On an anthropogenic timescale (yrs 1959-2020), the increasing CO_2-Sea Level- Temperature Anomaly trend is shown in figure 19.

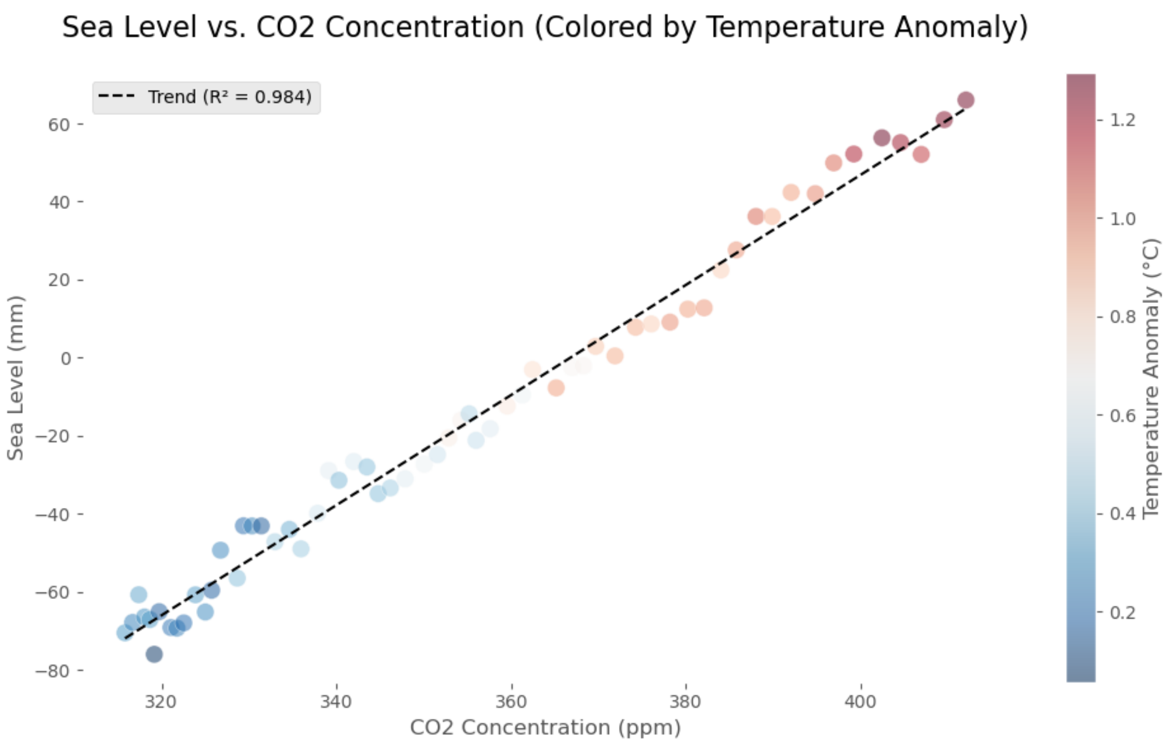

Figure 19. The correlation between variables of concern on Earth, over a few decades (1959-2020) with each data point corresponding to one year, with CO_2 as a hue, increasing every year. Higher CO_2 concentrations (Filtered annual data from Keeling et. al. [40]) are correlated with higher Sea Levels (As reported by Church 2011 and University Of Hawaii Sea Level Center) [41,42] and higher temperature anomalies (Data from: Met Office H. C. [43]).

6. Online Forecasting Models

Broccardo et al. [44] proposed a Bayesian model based on nonhomogeneous Poisson process (NHPP) to forecast induced seismicity. A successful decision-making criterion emerging from such model, would include effective engagement with communities to come up with mitigation plans. Such forecasting models can also be used in other areas of anthropogenic activities known to cause seismicity.

The probability of observing n_h seismic events in the time window $[t, t+h]$, given the observed data $D(t)$ up to time (t), $P(N_h(t) = n_h \mid D(t))$, or simply Ξ, is:

 doi:10.20944/preprints202504.2596.v3

$$\Xi = \int_\theta \left[\frac{\left(\int_t^{t+h} \lambda(t' \mid \theta)\, dt' \right)^{n_h}}{n_h!} \exp\left(- \int_t^{t+h} \lambda(t' \mid \theta)\, dt' \right) \right] f''_\theta(\theta \mid D(t))\, d\theta \tag{12}$$

Ξ represents the predictive probability of observing n_h seismic events in a future time window $[t, t+h]$, given observed data $D(t)$. Here, $N_h(t)$ is the number of events in the time window of interest, $\lambda(t' \mid \theta)$ is the time dependent seismicity rate which depends on model parameters θ and $\int_t^{t+h} \lambda(t' \mid \theta)\, dt'$ is the expectation value of the number of events in that interval. The first term is the Poisson probability of observing n_h events, given the rate.

The posterior distribution $f''_\theta(\theta \mid D(t))$ updates the knowledge about θ, using $D(t)$, and the integral over θ takes into account the uncertainties by averaging.

7. Discussions

Bayesian Inference certainly helps us better understand anthropogenic risks. Modern analysis tools such as the MCMC are therefore certainly useful in shedding light on contemporary problems in Earth Science and particularly inverse problems in geophysics.

Bayesian inference, however, is not a magic black box that could be used for compensating for poorly designed experiments and if information is primarily missing from data, no data analysis tools can reveal information out of thin air. That said, Bayesian inference could be used to better arrange for experimental setups to hunt for information that otherwise could not be captured [45]. This approach can even further improve geophysics experiments which could contribute to the understanding of Earth and planetary processes and anthropogenic risk factors in seismicity.

References

1. Turcotte, D.L.; Malamud, B.D. Earthquakes as a complex system. In *International Geophysics*; Elsevier, 2002; Vol. 81, pp. 209–cp1.
2. Sieh, K.; Stuiver, M.; Brillinger, D. A more precise chronology of earthquakes produced by the San Andreas fault in southern California. *Journal of Geophysical Research: Solid Earth* **1989**, *94*, 603–623.
3. Carpenter, B.; Marone, C.; Saffer, D. Weakness of the San Andreas Fault revealed by samples from the active fault zone. *Nature Geoscience* **2011**, *4*, 251–254.
4. Collettini, C.; Niemeijer, A.; Viti, C.; Marone, C. Fault zone fabric and fault weakness. *Nature* **2009**, *462*, 907–910.
5. Moore, D.E.; Rymer, M.J. Talc-bearing serpentinite and the creeping section of the San Andreas Fault. *Nature* **2007**, *448*, 795–797.
6. Scholz, C.H. Evidence for a strong San Andreas Fault. *Geology* **2000**, *28*, 163–166.
7. Vilarrasa, V.; Carrera, J.; Olivella, S.; Rutqvist, J.; Laloui, L. Induced seismicity in geologic carbon storage. *Solid Earth* **2019**, *10*, 871–892.
8. Walker, J.C.; Hays, P.; Kasting, J.F. A negative feedback mechanism for the long-term stabilization of Earth's surface temperature. *Journal of Geophysical Research: Oceans* **1981**, *86*, 9776–9782.
9. Penman, D.E.; Caves Rugenstein, J.K.; Ibarra, D.E.; Winnick, M.J. Silicate weathering as a feedback and forcing in Earth's climate and carbon cycle. *Earth-Science Reviews* **2020**, *209*, 103298. https://doi.org/https://doi.org/10.1016/j.earscirev.2020.103298.
10. Archer, D. Fate of fossil fuel CO2 in geologic time. *Journal of geophysical research: Oceans* **2005**, *110*.
11. Archer, D.; Eby, M.; Brovkin, V.; Ridgwell, A.; Cao, L.; Mikolajewicz, U.; Caldeira, K.; Matsumoto, K.; Munhoven, G.; Montenegro, A.; et al. Atmospheric lifetime of fossil fuel carbon dioxide. *Annual review of earth and planetary sciences* **2009**, *37*, 117–134.

 doi:10.20944/preprints202504.2596.v3

12. Colbourn, G.; Ridgwell, A.; Lenton, T. The time scale of the silicate weathering negative feedback on atmospheric CO2. *Global Biogeochemical Cycles* **2015**, *29*, 583–596.
13. Meissner, K.J.; McNeil, B.I.; Eby, M.; Wiebe, E.C. The importance of the terrestrial weathering feedback for multimillennial coral reef habitat recovery. *Global Biogeochemical Cycles* **2012**, *26*.
14. Batalha, N.E.; Kopparapu, R.K.; Haqq-Misra, J.; Kasting, J.F. Climate cycling on early Mars caused by the carbonate–silicate cycle. *Earth and Planetary Science Letters* **2016**, *455*, 7–13.
15. Laine, M. *Adaptive MCMC methods with applications in environmental and geophysical models*; Finnish Meteorological Institute, 2008.
16. Malinverno, A. Parsimonious Bayesian Markov chain Monte Carlo inversion in a nonlinear geophysical problem. *Geophysical Journal International* **2002**, *151*, 675–688.
17. Menke, W. *Geophysical data analysis: Discrete inverse theory*; Academic Press, 2018.
18. Sambridge, M.; Mosegaard, K. Monte Carlo methods in geophysical inverse problems. *Reviews of Geophysics* **2002**, *40*, 3–1.
19. Trotta, R. Bayes in the sky: Bayesian inference and model selection in cosmology. *Contemporary Physics* **2008**, *49*, 71–104.
20. Rahemi, R. Variation in electron work function with temperature and its effect on the Young's modulus of metals. *Scripta materialia* **2015**, *99*, 41–44.
21. Chang, J.; Nikolaev, P.; Carpena-Núñez, J.; Rao, R.; Decker, K.; Islam, A.E.; Kim, J.; Pitt, M.A.; Myung, J.I.; Maruyama, B. Efficient closed-loop maximization of carbon nanotube growth rate using Bayesian optimization. *Scientific reports* **2020**, *10*, 9040.
22. Uncertainty quantification of pollutant source retrieval: comparison of Bayesian methods with application to the Chernobyl and Fukushima Daiichi accidental releases of radionuclides **2017**. *143*, 2886–2901.
23. Sakuragi, Y.; Meason, J.L.; Kuroda, P.K. Uranium and plutonium isotopes in the atmosphere. *Journal of Geophysical Research* **1983**, *88*, 3718–3724. https://doi.org/10.1029/JC088iC06p03718.
24. Cluff, L. Photo Credit. Getty Images.
25. Menke, W. *Geophysical data analysis: Discrete inverse theory*; Academic Press, 2018.
26. Li, A. *Topics In Data Science: Data Analysis In Physics Lectures*; Halıcıoğlu Data Science Institute: La Jolla, California, 2025.
27. Savage, J.C.; Burford, R.O. Geodetic determination of relative plate motion in central California. *Journal of Geophysical Research* **1973**, *78*, 832–845.
28. Tong, X.; Sandwell, D.; Smith-Konter, B. High-resolution interseismic velocity data along the San Andreas Fault from GPS and InSAR. *Journal of Geophysical Research: Solid Earth* **2013**, *118*, 369–389.
29. IGPP. *Instituge Of Geophysics and Planatary Physics*; 2024.
30. MORZFELD, M. *Geophysical Data Analysis SIOG223- Class Notes*; 2024.
31. Rockwell, T.K.; Dawson, T.E.; Young Ben-Horin, J.; Seitz, G. A 21-event, 4,000-year history of surface ruptures in the Anza seismic gap, San Jacinto Fault, and implications for long-term earthquake production on a major plate boundary fault. *Pure and Applied Geophysics* **2015**, *172*, 1143–1165.
32. Biot, M.A. General theory of three-dimensional consolidation. *Journal of applied physics* **1941**, *12*, 155–164.
33. Hill, R.G.; Weingarten, M.; Rockwell, T.K.; Fialko, Y. Major southern San Andreas earthquakes modulated by lake-filling events. *Nature* **2023**, *618*, 761–766.
34. Human-Induced Earthquake Database (HiQuake). Induced Earthquakes, 2025. Accessed: 2025-04-27.
35. Talwani, P. On the nature of reservoir-induced seismicity. *Pure and applied Geophysics* **1997**, *150*, 473–492.
36. Deng, F.; Dixon, T.H.; Xie, S. Surface deformation and induced seismicity due to fluid injection and oil and gas extraction in western Texas. *Journal of Geophysical Research: Solid Earth* **2020**, *125*, e2019JB018962.
37. Argus, D.F.; Heflin, M.B.; Peltzer, G.; Crampé, F.; Webb, F.H. Interseismic strain accumulation and anthropogenic motion in metropolitan Los Angeles. *Journal of Geophysical Research: Solid Earth* **2005**, *110*.
38. of the Interior, U.D. National Assessment of Geologic Carbon Dioxide Storage Resources-Data. Technical report, 2013.
39. Melini, D.; Piersanti, A. Impact of global seismicity on sea level change assessment. *Journal of Geophysical Research: Solid Earth* **2006**, *111*.
40. Keeling, C.D.; Piper, S.C.; Bacastow, R.B.; Wahlen, M.; Whorf, T.P.; Heimann, M.; Meijer, H.A. Exchanges of atmospheric CO2 and 13CO2 with the terrestrial biosphere and oceans from 1978 to 2000. I. Global aspects. SIO Reference Series 01-06, Scripps Institution of Oceanography, San Diego, 2001.

 doi:10.20944/preprints202504.2596.v3

41. Church, J.A.; White, N.J.; Konikow, L.F.; Domingues, C.M.; Cogley, J.G.; Rignot, E.; Gregory, J.M.; van den Broeke, M.R.; Monaghan, A.J.; Velicogna, I. Revisiting the Earth's sea-level and energy budgets from 1961 to 2008. *Geophysical Research Letters* **2011**, *38*.
42. University of Hawaii Sea Level Center. UHSLC – University of Hawaii Sea Level Center, 2025. Accessed: 2025-04-27.
43. Met Office Hadley Centre and Climatic Research Unit. HadCRUT5: Global historical surface temperature anomalies dataset, 2025. Version HadCRUT.5.0.2.0, Accessed: 2025-04-27.
44. Broccardo, M.; Mignan, A.; Wiemer, S.; Stojadinovic, B.; Giardini, D. Hierarchical Bayesian modeling of fluid-induced seismicity. *Geophysical Research Letters* **2017**, *44*, 11–357.
45. Von Toussaint, U. Bayesian inference in physics. *Reviews of Modern Physics* **2011**, *83*, 943–999.